Isopycnal eddy stirring dominates thermohaline mixing in the upper subpolar North Atlantic

Bieito Fernández Castro[1], Daniel Fernández Román[2], Bruno Ferron[3], Marcos Fontela[4], Pascale Lherminier[3], Alberto Naveira Garabato[1], Fiz F. Pérez[4], Carl Spingys[5], Kurt Polzin[6], and Antón Velo[4]

[1]Ocean and Earth Science, National Oceanography Centre, University of Southampton, Southampton, UK
[2]Centro de Investigacións Mariñas, Universidade de Vigo (CIM-UVigo), Vigo, Spain
[3]Univ Brest, CNRS, Ifremer, IRD, Laboratoire d'Océanographie Physique et Spatiale (LOPS), IUEM, F29280, Plouzané, France
[4]Instituto de Investigacións Mariñas, IIM-CSIC, Vigo, Spain
[5]National Oceanography Centre, Southampton, UK
[6]Woods Hole Oceanographic Institution, Woods Hole, USA

Key Points:

- We quantify diapycnal and isopycnal contributions to thermohaline mixing in the subpolar North Atlantic with microstructure observations
- Isopycnal stirring dominates thermohaline mixing suggesting a key role in the water-mass transformations driving the overturning circulation
- The relative importance of isopycnal stirring is tracer-dependent, controlled by the large-scale co-variability of the tracer with density

Corresponding author: Bieito Fernández Castro, `b.fernandez-castro@soton.ac.uk`

Abstract

The Atlantic Meridional Overturning Circulation (AMOC) entails vigorous thermohaline transformations in the subpolar North Atlantic (SPNA). There, warm and saline waters originating in the subtropics are converted into cooler and fresher waters by a combination of surface fluxes and sub-surface thermohaline mixing. Using microstructure measurements and a small-scale variance conservation framework, we quantify the diapycnal and isopycnal contributions to thermohaline mixing within the eastern SPNA. Isopycnal stirring is found to account for 65% of thermal and 84% of haline variance dissipation in the upper 400 m of the eastern SPNA, suggesting an important role of isopycnal stirring in regional water-mass transformations. By applying the tracer variance method to two tracers, we underscore the special significance of isopycnal stirring for tracers weakly coupled to density, such as biologically-active tracers. Our findings thus highlight the central role of isopycnal stirring in both the AMOC and biogeochemical dynamics within the SPNA.

Plain Language Summary

The North Atlantic hosts an ocean circulation system called the Atlantic Meridional Overturning Circulation (AMOC). It is often likened to a giant conveyor belt in the ocean, moving warm, salty waters from south to north and transforming them into cold, fresh waters that flow back southward within the deep ocean. The AMOC is a crucial element of the Earth's climate, and if it were to slow down, it could lead to major climatic changes. For a long time, scientists thought that the AMOC was mainly driven by cooling in the North Atlantic. But recently, we have discovered that the mixing of different water masses is also important. In our study, we used small-scale measurements of ocean properties to examine the processes behind this mixing. Our findings show that large swirling flows known as mesoscale eddies, which are tens to hundreds of kilometers wide and hundreds of meters deep, play a dominant role in mixing heat and salt in the North Atlantic. This discovery helps us to better understand the AMOC and its future behavior.

1 Introduction

The subpolar North Atlantic (SPNA) is a hotspot of ocean ventilation, resulting in significant exchanges of heat and greenhouse gases with the atmosphere (Pérez et al., 2013). This makes the SPNA an important region in the regulation of Earth's climate. The climatic relevance of the SPNA is rooted in its central role in the global meridional overturning circulation (MOC) (Daniault et al., 2016; Lozier et al., 2019). Within the cyclonic pathways of the SPNA gyre, vigorous water mass transformations convert warm and salty subtropical central waters into cooler, fresher and denser subpolar mode waters (SPMW) (Brambilla & Talley, 2008; García-Ibáñez et al., 2015) and intermediate waters. These intermediate waters are formed through deep convection in the Irminger (Pickart et al., 2003; De Jong et al., 2012) and Labrador seas (Lazier et al., 2002). Together with denser overflows from the Nordic Seas, SPNA-produced waters constitute the lower limb of the Atlantic MOC (AMOC), which flows southward within a Deep Western Boundary Current along the North American margin (Daniault et al., 2016; Lozier et al., 2019).

Traditionally, deep convection in the Labrador Sea was considered the primary source of dense water for the AMOC. Recent observations, however, have led to a paradigm shift, by which the majority of the light-to-dense water mass conversion driving the AMOC is recognised to occur in the eastern SPNA (eSPNA), specifically in the Irminger Sea, and the Nordic Seas (Mauritzen, 1996; Daniault et al., 2016; Lozier et al., 2019; Petit et al., 2020). Further, while conventional understanding views the AMOC as an intrinsically diapycnal process, recent investigations suggest that water-mass transformations in the SPNA involve large density-compensated (isopycnal) temperature and salinity changes (Zou et al., 2020; Evans et al., 2023).

Finally, closure of the AMOC in the SPNA has been traditionally attributed to atmospheric cooling (Marsh, 2000; Petit et al., 2020), yet there is growing evidence that interior thermohaline transformations, driven by mixing along and across density surfaces, are necessary for sustaining the AMOC (Xu et al., 2018; Brüggemann & Katsman, 2019; Mackay et al., 2020; Evans et al., 2023; Tooth et al., 2023; Bebieva & Lozier, 2023). Diapycnal mixing contributes, for example, to the densification of SPMW through entrainment of overflow waters (Evans et al., 2023). In turn, isopycnal stirring delivers salt into the subpolar gyre, enabling an increase in the density of lower-limb waters (Warren, 1983; Pradal & Gnanadesikan, 2014; Born et al., 2016; Evans et al., 2023); and delivers intermediate waters produced by deep convection in the Labrador and Irminger basins into the Deep Western Boundary Current, thereby connecting such waters to the AMOC (Straneo, 2006; Brüggemann & Katsman, 2019; Mackay et al., 2020).

Despite the increasingly acknowledged importance of interior thermohaline transformations in the SPNA, direct observations in the area are scarce (Lauderdale et al., 2008; Ferron et al., 2014), and quantification relies largely on indirect mixing estimates via inverse methods and model output analyses (Xu et al., 2018; Mackay et al., 2020; Evans et al., 2023; Tooth et al., 2023). Consequently, the nature of the processes driving these transformations remains largely unknown. Mixing – the destruction of property contrasts by molecular diffusion– results from a downscale variance cascade driven by the stirring of isopycnal property gradients by mesoscale eddies (horizontal scale > 10 km), and the mixing of diapycnal property gradients by small-scale turbulence (horizontal and vertical scales < 10 m)(Lee et al., 1997; Garrett, 2001; Ferrari & Polzin, 2005; Naveira Garabato et al., 2016). The small- and mesoscale regimes are underpinned by different dynamics, and are likely to exhibit distinct sensitivities to changes in forcing and potential feedbacks on the AMOC. A deeper understanding of SPNA mixing processes is thus essential for unravelling the AMOC's dynamics and long-term evolution.

In this study, we address the role of mixing in SPNA thermohaline transformations by analyzing a set of microstructure temperature and shear profiles, collected across the eSPNA, within a tracer variance budget framework (Ferrari & Polzin, 2005; Naveira Garabato et al., 2016). Our analysis reveals that mesoscale stirring dominates thermal and, more distinctly, haline mixing in the upper layers of the eSPNA, indicating and important contribution of mesoscale turbulence to the water-mass transformations driving SPMW production and the AMOC's closure in the SPNA.

2 Dataset

Microstructure data were collected during the BOCATS2 2023 cruise across the North Atlantic Ocean from 9th June to 11th July 2023. The mission sampled the OVIDE repeated hydrography section (WOCE A25) between Portugal and Cape Farewell (Greenland) (Lherminier et al., 2010, 2023), and two additional sections across the East Greenland Current (EGC) and the Irminger Sea, north of the A25-OVIDE line (Fig.1a). Microstructure turbulence profiles were collected in 32 stations with a microstructure profiler (MSS, Prandke and Stips (1998)). A total of 94 profiles were obtained, with 1-3 profiles per station, except in the last station (station 32) over the Reykjanes Ridge at 61.14°N, 27.97°. There, a time-series consisting of 21 profiles was recorded during a 14-hour period (TS label in Fig.1a). Profiles were performed down to depths of 300-400 m, except in shallower stations of the EGC.

The MSS is equipped with two shear microstructure sensors and a temperature microstructure sensor, complemented with a Sea&Sun high-accuracy Conductivity-Temperature-Depth (CTD) suite. The instrument is loosely-tethered and operated in free-falling mode at a vertical speed of 0.6–0.7 m s^{-1}, and samples all variables at 1024 Hz. Profiles of potential temperature (θ), practical salinity (S) and surface-referenced potential density (σ_θ) with 1 m vertical resolution were derived by bin-averaging the CTD output. The dissipation rates of turbulent kinetic energy (ε) and thermal variance (χ) were computed from the microstructure shear and temperature measurements, respectively, with a vertical resolution of 1 m from overlapping data segments of 4 m length following Piccolroaz et al. (2021); Fernández Castro et al. (2022).

Generally, ε and χ_θ were determined by integration of the shear and temperature gradient spectra over the well-resolved wavenumber ranges, and the variance outside those ranges was recovered using empirical spectral forms (Nasmyth and Kraichnan, respectively) (Fernández Castro et al., 2022) (Fig. S1). Due to weak turbulence, shear-based ε estimates occasionally approached the instrument's noise floor of $\mathcal{O}(10^{-9}\,\mathrm{W/kg})$. In those instances, ε was derived through fitting the temperature gradient spectrum to the Kraichnan spectrum (Piccolroaz et al., 2021), as this technique has a lower noise floor of $\mathcal{O}(10^{-12}\,\mathrm{W/kg})$. For consistency, in those instances χ_θ was also derived from spectral fits.

3 Triple decomposition of the tracer variance budget

3.1 Background

To investigate the relative contribution of small- and mesoscale turbulence to thermohaline mixing, we followed a triple decomposition of the small-scale tracer variance conservation equation (Joyce, 1977; Davis, 1994; Garrett, 2001; Ferrari & Polzin, 2005). In the limit of flow and tracer fluctuations (here we use potential temperature, θ, as our reference tracer) being statistically stationary and homogeneous, the equation for tracer variance conservation in a traditional two-term Reynolds decomposition framework can be expressed as:

$$\underbrace{-2\overline{\mathbf{u}^t\theta^t}\cdot\nabla\overline{\theta}}_{P_{\theta^2}} = \underbrace{2\kappa_\theta\overline{(\nabla\theta^t)^2}}_{\chi_\theta} \tag{1}$$

where $\mathbf{u}$ is the flow velocity, ∇ is a three-dimensional gradient operator, and κ_θ is the molecular diffusivity of heat. This equation expresses a local balance between the production of small-scale tracer variance, P_{θ^2}, due to the stirring of the larger-scale three-dimensional tracer gradient (∇) by turbulent eddies, and its dissipation by molecular diffusion, χ_θ. Here, the double decomposition implies a scale separation between the "mean" flow ($\bar{\cdot}$) and the "turbulent" fluctuations ($\cdot^t$). In oceanographic studies, turbulent fluctuations are defined as those related to small-scale three-dimensional turbulence (smaller than a few meters in the vertical), which results in diapycnal mixing. The mean flow thus covers multi-meter length scales, which are resolved by standard (CTD) oceanographic measurements, and includes the basin-scale tracer contrasts, but also fine-scale structures due to stirring by mesoscale motions along isopycnal surfaces (Ferrari & Polzin, 2005).

By taking a gradient flux approximation ($\overline{\mathbf{u}^t\theta^t} = -K_\rho \nabla\overline{\theta}$), and using the facts that diapycnal gradients are much larger than isopycnal gradients and isopycnal layers are close to horizontal ($|\nabla\overline{\theta}| \approx |\partial\overline{\theta}/\partial z|$), tracer variance dissipation can be related to a small-scale turbulent diapycnal diffusivity (K_ρ) through the Osborn and Cox (1972) formula:

$$\chi_\theta = P_{\theta^2} \approx 2K_\rho \left(\frac{\partial\overline{\theta}}{\partial z}\right)^2 \tag{2}$$

In order to separately account for the role of mesoscale eddies in driving the downscale variance cascade, the triple decomposition additionally decomposes the mean quantities into a large-scale mean component ($\cdot^m$) and a mesoscale eddy component ($\cdot^e$), $\overline{\theta} = \theta^m + \theta^e$, yielding (Ferrari & Polzin, 2005):

$$\underbrace{-2\langle \mathbf{u}^t\theta^t\rangle \cdot \nabla_\perp \theta^m}_{P^\perp_{\theta^2}} \underbrace{-2\langle \mathbf{u}^e\theta^e\rangle \cdot \nabla_{||}\theta^m}_{P^{||}_{\theta^2}} = \chi_\theta \tag{3}$$

where angled brackets represent an average over spatial scales large in comparison with mesoscale fluctuations, but small in comparison with the large-scale mean flow; $\nabla_\perp$ and $\nabla_{||}$, respectively, denote gradient operators across and along density surfaces. Here, the dissipation of thermal variance is balanced by the stirring of the mean diapycnal gradient by small-scale turbulence ($P^\perp_{\theta^2}$) plus the stirring of the large-scale isopycnal gradients by mesoscale motions ($P^{||}_{\theta^2}$). By applying a flux-gradient relationship, $P^\perp_{\theta^2}$ can be linked to the small-scale diapycnal diffusivity:

$$P^\perp_{\theta^2} = 2K_\rho(\nabla_\perp\theta^m)^2, \tag{4}$$

and the contribution of eddy stirring to mixing can be diagnosed as:

$$P^{||}_{\theta^2} = \chi_\theta - P^\perp_{\theta^2} = \chi_\theta - 2K_\rho(\nabla_\perp\theta^m)^2. \tag{5}$$

3.2 Implementation

By applying the variance budget framework (Eqs. 3-5) to BOCATS2 microstructure data, we assess the relative contribution of small-scale turbulence and mesoscale stirring to thermohaline mixing. To estimate $P^\perp_{\theta^2}$ (and $P^\perp_{S^2}$) from equation 4, the measured $\overline{\theta}$ (and $\overline{S}$) profiles were smoothed through a 4-degree polynomial fit against σ_θ to remove the density-compensated fine-scale structures ($\mathcal{O}(10-100\,\mathrm{m})$ length scales) associated with isopycnal stirring and obtain the "mean flow" θ^m and S^m profiles:

$$\theta^m = f(a_0 + a_1 \cdot \sigma_\theta + \ldots + a_4 \cdot \sigma_\theta^4) \tag{6}$$

Although the choice of a 4-degree polynomial is somewhat arbitrary, our results prove relatively insensitive to that choice. The diapycnal diffusivity was calculated using the Osborn (1980) formula:

$$K_\rho = \Gamma \frac{\varepsilon}{\overline{N}^2} \tag{7}$$

where $\Gamma = 0.2$ is a mixing efficiency (Oakey, 1982; St Laurent & Schmitt, 1999; Ijichi et al., 2020), and $\overline{N}^2 = -g/\rho\partial\bar{\rho}\partial z$ is the buoyancy frequency. The density gradient is calculated by linear fitting the measured density profile against depth over 4 m segments.

While thermal variance dissipation rate (χ_θ) is obtained directly from observed microstructure temperature gradients, we have no equivalent measurements available to estimate χ_S. We circumvent this issue with a new approach using the Osborn and Cox (1972) formula (Eq. 2) to estimate χ_S from K_ρ and the fine-scale vertical salinity gradient as measured by the CTD ($\partial\overline{S}/\partial z$):

$$\chi_S \approx 2K_\rho \left(\frac{\partial\overline{S}}{\partial z}\right)^2, \tag{8}$$

where $\partial\overline{S}/\partial z$ is determined by linear fitting over 4 m segments. This approximation assumes that χ_S is balanced locally by the effect of stirring by small-scale turbulence on fine-scale tracer gradients (P_{S^2}) and is supported by the good agreement (mostly within a factor of 2) between χ_θ and P_{θ^2} over 5 orders of magnitude (Fig. 2).

4 Results

4.1 Hygrography

The BOCATS2 microstructure survey stations covered the broad range of hydrographic conditions characterising the eSPNA, which reflect the transformation of subtropical central waters into SPMW (García-Ibáñez et al., 2015). The eastern section (stations 1-10) sampled the relatively warm (10-20 °C, Fig. 1b), salty ($>$ 35.5 PSU, Fig. 1c) and light ($\sigma_\theta < 27.4$ kg/m^3) subtropical waters of the Western European Basin (WEB). The upper ocean (<400 m) of the WEB was strongly stratified, with a $\sim$1 kg/m^3 contrast between the upper and deeper sampled layers (Fig. 1d,e). WEB stratification was dominated by temperature differences, whilst haline stratification was weakly unstable (Fig. 1a,b,e). The western sections sampled across the Irminger Sea (IrmS) and the East Greenland Current (EGC). Below a shallow seasonal thermocline, IrmS waters were cooler (3-11 °C, Fig. 1b) and fresher (35.0-35.5 PSU, Fig. 1c) than WEB waters, and also denser, with $\sigma_\theta > 27.5$ kg/m^3, as is characteristic of SPMW (Fig. 1d). The upper IrmS was also thermally stratified, but more weakly than the WEB, with a density difference of $\sim$0.7 kg/m^3 (Fig. 1e). The salinity profiles were rather homogeneous (Fig. 1c), resulting in very weak haline stratification (Fig. 1e). Finally, the offshore waters of the EGC showed a large overlap in thermohaline properties with IrmS waters, at least below 100 m depth. However, shallower waters were markedly cooler, fresher and lighter, particularly in the inner EGC, with temperatures and salinities as low as -1°C and 30 PSU (Fig. 1b,c). Contrary to the WEB and IrmS, the strong stratification of EGC waters (>1 kg/m^3 in inshore stations) was salinity-driven (Fig. 1e).

Overall, BOCATS2 sampled across a northwestward gradient of decreasing temperature and salinity, which is partially density-compensated. This partial compensation allows the existence of substantial thermohaline gradients along isopycnals (Fig. 1a). Mesoscale eddies acting on these large-scale thermohaline gradients produce measurable density-compensated thermohaline fine-scale vertical structures (Fig. 1b,c). Such fine structures make different contributions to the overall θ and S vertical variance in different regions (Fig. 1f), reflecting the relative importance of isopycnal stirring. Due to the strong thermal stratification in the WEB and IrmS, almost 100% of the θ vertical variance corresponds to the mean profile (θ^m), although thermal fine-scale structures were also evident there (Fig. 1b). Fine-scale structures had a larger imprint on salinity vertical variance in those same regions, where the mean salinity profile (S^m) contained only 50-80% of the S variance, due to the weak salinity stratification. The reverse scenario was encountered in the salinity-stratified EGC region, where most of S variance was explained by S^m, and θ fine structures made a variable but larger (up to 50%) contribution to thermal variance.

4.2 Isopycnal stirring and diapycnal mixing from a time-series station

The occurrence of density-compensated thermohaline fine-structures, and their temporal variability, is clearly illustrated in the time-series station data at the Reykjanes Ridge (Fig. 3a,b). As the rest of the IrmS, the sampling site was thermally-stratified with a thermocline at around 50 m depth (Fig. 3a), while salinity did not exhibit a well-defined mean vertical structure. Instead, there was substantial temporal and vertical fine-scale variability (Fig. 3b). Although some isopycnal heaving was apparent, thermohaline variability occurred mostly at constant density, as salinity anomalies were mirrored by opposing temperature anomalies (Figs. 3a,b, S2, S3). The site was rather turbulent, with ε and χ_θ values of $10^{-8} - 10^{-7}$ W/kg and $10^{-7} - 10^{-6}$ K^2/s in the surface layer and thermocline, and recurrent patches of comparably intense turbulence and mixing in deeper layers (Fig. 3a,b).

The mean rates of thermal variance dissipation (χ_θ) and diapycnal production ($P^{\perp}_{\theta^2}$, Eq. 4), were similar at 10^{-7} K^2/s in the shallow thermocline (Fig. 3c), indicating a dominance of thermal mixing by small-scale turbulence. However, below 100 m depth, χ_θ was consistently higher than $P^{\perp}_{\theta^2}$, due to the intensification of thermal mixing associated with fine-scale eddy-induced variability. When averaged below 100 m, $P^{\perp}_{\theta^2}$ (0.15×10^{-8} K^2/s), accounted for about one third of the overall χ_θ (0.49×10^{-8} K^2/s). Therefore, eddy stirring was the main driver of thermal mixing below the seasonal thermocline. Due to the lack of a well-defined mean diapycnal salinity gradient, the contribution of eddy stirring to salinity mixing was overwhelmingly dominant, even within the thermocline (Fig. 3d), as diapycnal production ($P^{\perp}_{S^2} = 0.16 \times 10^{-11}$ PSU^2/s) explained only 1.3% of the haline variance dissipation ($\chi_S = 1.27 \times 10^{-10}$ PSU^2/s).

4.3 Regional patterns in isopycnal stirring and diapycnal mixing

The analysis of all the microstructure profiles recorded during BOCATS2 was consistent with the overall dominance of mesoscale stirring below the seasonal pycnocline ($\sim$100 m), for both temperature and salinity mixing (Fig. 4a,f). On average, small-scale turbulence accounted for 36% of the observed mean χ_θ (1.82×10^{-8} K^2/s), and for 16% of the mean χ_S (0.64×10^{-9} PSU^2/s). The cruise-mean values encapsulate substantial regional differences in both the intensity of mixing and the relative importance of diapycnal and isopycnal processes.

At the WEB, mixing below the seasonal thermocline was weaker than the cruise mean, at $\chi_\theta = 0.39 \times 10^{-8}$ K^2/s and $\chi_S = 2.86 \times 10^{-10}$ PSU^2/s, respectively. In this thermally stratified basin, diapycnal production was sufficient to explain almost all (78%) of the observed thermal mixing, while its contribution to salinity mixing was close to the cruise-average value of 15% (Fig. 4b,g). The IrmS was characterised by intermediate variance destruction rates of $\chi_\theta = 1.21 \times 10^{-8}$ K^2/s and $\chi_S = 3.67 \times 10^{-10}$ PSU^2/s, respectively, and a dominant role of isopycnal stirring, as diapycnal production accounted for only 19% and 0.6% of the thermal and haline mixing, respectively (Fig. 4c,h). At the EGC region, where turbulent kinetic energy dissipation rates were large (Fig. 1), the highest levels of mixing were observed at $\chi_\theta = 8.07\times10^{-8}$ K^2/s and $\chi_S = 27.0\times10^{-10}$ PSU^2/s, respectively. In this salinity-stratified area, the relative contribution of diapycnal haline mixing was the highest of the cruise at 25%. The mean contribution of diapycnal mixing to thermal variance dissipation sat at intermediate values of 40% below the halocline. However, within the halocline, thermal mixing was largely associated with isopycnal stirring, consistent with the sharp fine-scale thermal structures observed there (Fig. 1b).

5 Discussion

In our study, we leveraged a set of summertime microstructure observations in the eSPNA to assess the rates of variance dissipation by small-scale diapycnal mixing and mesoscale eddy stirring, respectively. While employing microstructure observations for investigating diapycnal mixing is a well-established technique in modern oceanography (Waterhouse et al., 2014), the quantification of isopycnal stirring using this approach remains relatively underexplored, with only a few notable exceptions (Ferrari & Polzin, 2005; Naveira Garabato et al., 2016; Orúe-Echevarría et al., 2023). Building upon this work, we base our analysis on a triple decomposition of the tracer variance conservation equation, along with measurements of ε and χ_θ. Additionally, we extend previous efforts by applying the triple decomposition to the salinity variance budget, by using the Osborn and Cox (1972) equation to estimate χ_S. An quantification of the methodological uncertainties is presented in the supplementary material.

Our analysis unveiled the dominance of mesoscale stirring in driving mixing of heat and salt across subtropical central water and SPMW layers of the upper eSPNA. These findings align with previous results derived from reanalysis and modeling datasets (Xu et al., 2018; Tooth et al., 2023), which emphasize the role of lateral mixing along the polar front in transforming subtropical waters into SPMW, a key component of the AMOC (Evans et al., 2023). Our measurements further indicate that the dominance of mesoscale processes is widespread, particularly in the Irminger Sea, extending beyond frontal regions. The highest rates of energy and variance dissipation were measured at the EGC, in line with previous observations (Lauderdale et al., 2008). Despite intense small-scale turbulence, isopycnal stirring was also the main driver of mixing at the EGC, accounting for >50% of heat and salt variance dissipation. This finding is consistent with vigorous property exchanges between the ventilated basin interior and boundary currents, demonstrated in idealized and realistic simulations and observations (Straneo, 2006; Brüggemann & Katsman, 2019; Mackay et al., 2020; Le Bras et al., 2020). Such exchange is considered a critical element of the AMOC. However, it must be noted that our measurements have limited spatio-temporal coverage, and a full quantitative assessment of the significance of mixing for the AMOC, which would require sampling all seasons, was not possible.

Beyond the general dominance of isopycnal stirring, we observed substantial tracer-dependent regional variations in the relative importance of diapycnal and isopycnal proceseses across the eSPNA. These regional patterns appear to be primarily driven by the degree of co-variability between large-scale tracer and density distributions. In regions where the considered tracer is the primary driver of vertical density stratification, and thus highly correlated with density, diapycnal mixing plays a more prominent role. For instance, thermal mixing is predominantly diapycnal in the thermally stratified WEB, and isopycnal in the EGC's halocline, where diapycnal mixing makes the largest contribution to salinity variance dissipation. In the Irminger Sea, where vertical density stratification is relatively weak, mixing is facilitated by the existence of isopycnal gradients, enhanced by regional ventilation and the confluence of water masses from the Arctic and subtropics (Evans et al., 2023), leading to a dominant role of mesoscale turbulence. This dominance is more pronounced for salinity, which exhibits small diapycnal gradients.

The prevalence of diapycnal temperature mixing in the subtropically-influenced WEB aligns with the temperature variance budget of the subtropical thermocline at the North Atlantic Tracer Release Experiment (NATRE) site (25°N, 30°W) (Ferrari & Polzin, 2005). In contrast to temperature, salinity mixing in the WEB is governed by isopycnal stirring. It is possible that the substantial role of isopycnal stirring is specific to the WEB's location within the subpolar gyre, where strong isopycnal gradients exist, rather than representing a general characteristic of the subtropical thermocline. However, strong isopycnal property gradients and evidence for isopycnal ventilation in the lower subtropical thermocline were also reported further south in the Azores region (Robbins et al., 2000).

The importance of isopycnal stirring in the SPMW layers of the Irminger Sea is consistent with thermal variance budget analyses in intermediate and deep waters of the Drake Passage and the Malvinas Confluence in the Southern Ocean (Naveira Garabato et al., 2016; Orúe-Echevarría et al., 2023). Our results endorse the hypothesis that properties in water masses outcropping at high latitudes are preferentially mixed along isopycnals (Naveira Garabato et al., 2017), while diapycnal mixing would be more important in the subtropical thermocline. It also emerges clearly that the relative importance of either process is strongly tracer-dependent, as well as region-dependent, yet current knowledge about this variability remains limited. A large-scale investigation of the relative importance of isopycnal stirring and diapycnal mixing would enhance our understanding of how the ocean interior is ventilated.

6 Conclusions

Using microstructure observations and a small-scale tracer variance conservation framework, our study has demonstrated that isopycnal stirring by mesoscale turbulence is the primary driver of heat and salt mixing in the upper eastern subpolar North Atlantic, at least during the summer season. Our findings are consistent with an important role of mixing in the formation of subpolar mode waters from subtropical waters, which contributes to the AMOC, and emphasize the strong isopycnal nature of these transformations, a facet often overlooked in the conventional perception of the AMOC as a primarily diapycnal phenomenon.

Isopycnal stirring emerges as a particularly crucial mechanism for salinity mixing, with potential implications for the transport of salt to the subpolar gyre, a factor directly impacting the AMOC by preconditioning the region for deep wintertime convection (Warren, 1983; Pradal & Gnanadesikan, 2014; Born et al., 2016). The assessment of mesoscale stirring's importance takes on new significance, especially in predicting how the AMOC might respond to increased freshwater input from melting ice (Ditlevsen, 2023). Despite the substantial challenge of quantifying isopycnal stirring from oceanographic observations (Abernathey et al., 2022), the application of the variance budget method considered here, along with the deployment of autonomous platforms like profiling floats equipped with turbulence sensors (Roemmich, 2019), offers a promising avenue for addressing this challenge and advancing our comprehension of the climatic role of ocean mixing.

Further, our extension of the small-scale variance budget method to tracers beyond temperature has unveiled the tracer-dependent nature of isopycnal stirring's relative significance. This point is particularly relevant for tracers whose large-scale distribution is uncoupled from density, such as salinity in a temperature-stratified ocean and temperature in a salinity-stratified ocean. The decoupling from density becomes more significant for tracers with biological sources or sinks, underscoring the central role of isopycnal stirring in the ocean's biogeochemical cycles (Abernathey & Ferreira, 2015; Bahl et al., 2019; Spingys et al., 2021). Investigating this phenomenon could be pursued by applying the variance budget method to data from an expanding fleet of biogeochemical Argo floats (Bittig, 2019; Roemmich, 2019), in conjunction with direct or indirect estimates of diapycnal mixing rates (Whalen, 2012).

7 Open Research

Hydographic and microstructure data collected during the BOCATS2 cruise are available at SEANOE (https://doi.org/10.17882/95607), associated resources can be found at UTM Data Centre (https://doi.org/10.20351/29SG20230608). The scripts used for microstructure data processing are available at ZENODO (Fernández Castro, 2023).

Acknowledgments

This research was supported by BOCATS2 (PID2019-104279GB-C21) project funded by MCIN/AEI/10.13039/501100011033 and by EuroGO-SHIP project (Horizon Europe #101094690). BFC is supported by NERC grants NE/W009528/1 and NE/Y002709/1. MF was funded by Juan de La Cierva Formación (FJC2019-038970-I, Ministerio de Ciencia e Innovación, Spanish Government). DFR was supported by a FPU predoctoral fellowship (FPU2021/04749) from the Spanish Ministerio de Universidades. We thank the crew members of the R/V Sarmiento de Gamboa and the technicians for their work at sea.

References

Abernathey, R., & Ferreira, D. (2015). Southern Ocean isopycnal mixing and ventilation changes driven by winds. *Geophysical Research Letters*, *42*(23). doi: 10.1002/2015GL066238

Abernathey, R., Gnanadesikan, A., Pradal, M.-A., & Sundermeyer, M. A. (2022). Isopycnal mixing. In *Ocean Mixing* (pp. 215–256). Elsevier. doi: 10.1016/B978-0-12-821512-8.00016-5

Bahl, A., Gnanadesikan, A., & Pradal, M. (2019). Variations in Ocean Deoxygenation Across Earth System Models: Isolating the Role of Parameterized Lateral Mixing. *Global Biogeochemical Cycles*, *33*(6), 703–724. doi: 10.1029/2018GB006121

Bebieva, Y., & Lozier, M. S. (2023). Fresh Water and Atmospheric Cooling Control on Density-Compensated Overturning in the Labrador Sea. *Journal of Physical Oceanography*, *53*(11), 2575–2589. doi: 10.1175/JPO-D-22-0238.1

Bittig, H. C. (2019). A BGC-Argo Guide: Planning, Deployment, Data Handling and Usage. *Frontiers in Marine Science*, *6*, 502. doi: 10.3389/fmars.2019.00502

Born, A., Stocker, T. F., & Sandø, A. B. (2016). Transport of salt and freshwater in the Atlantic Subpolar Gyre. *Ocean Dynamics*, *66*(9), 1051–1064. doi: 10.1007/s10236-016-0970-y

Brambilla, E., & Talley, L. D. (2008). Subpolar Mode Water in the northeastern Atlantic: 1. Averaged properties and mean circulation. *Journal of Geophysical Research*, *113*, C04025. doi: 10.1029/2006JC004062

Brüggemann, N., & Katsman, C. A. (2019). Dynamics of Downwelling in an Eddying Marginal Sea: Contrasting the Eulerian and the Isopycnal Perspective. *Journal of Physical Oceanography*, *49*(11), 3017–3035. doi: 10.1175/JPO-D-19-0090.1

Daniault, N., Mercier, H., Lherminier, P., Sarafanov, A., Falina, A., Zunino, P., ... Gladyshev, S. (2016). The northern North Atlantic Ocean mean circulation in the early 21st century. *Progress in Oceanography*, *146*, 142–158. doi: 10.1016/j.pocean.2016.06.007

Davis, R. E. (1994). Diapycnal Mixing in the Ocean: The Osborn–Cox Model. *Journal of Physical Oceanography*, *24*(12), 2560 – 2576. doi: 10.1175/1520-0485(1994)024⟨2560:DMITOT⟩2.0.CO;2

De Jong, M. F., Van Aken, H. M., Våge, K., & Pickart, R. S. (2012). Convective mixing in the central Irminger Sea: 2002–2010. *Deep Sea Research Part I: Oceanographic Research Papers*, *63*, 36–51. doi: 10.1016/j.dsr.2012.01.003

Ditlevsen, P. (2023). Warning of a forthcoming collapse of the Atlantic meridional overturning circulation. *Nature Communications*, *14*, 4254. doi: 10.1038/s41467-023-39810-w

Evans, D. G., Holliday, N. P., Bacon, S., & Le Bras, I. (2023). Mixing and air–sea buoyancy fluxes set the time-mean overturning circulation in the subpolar North Atlantic and Nordic Seas. *Ocean Science*, *19*(3), 745–768. doi: 10.5194/os-19-745-2023

Fernández Castro, B. (2023). *[Software] Microstructure processing code (MSS) - BOCATS2 cruise.* Zenodo. doi: 10.5281/zenodo.10267840

Fernández Castro, B., Peña, M., Nogueira, E., Gilcoto, M., Broullón, E., Comesaña, A., ... Mouriño-Carballido, B. (2022). Intense upper ocean mixing due to large aggregations of spawning fish. *Nature Geoscience*, *15*(4), 287–292. doi:

10.1038/s41561-022-00916-3

Ferrari, R., & Polzin, K. L. (2005). Finescale Structure of the T–S Relation in the Eastern North Atlantic. *Journal of Physical Oceanography*, *35*(8), 1437–1454. doi: 10.1175/JPO2763.1

Ferron, B., Kokoszka, F., Mercier, H., & Lherminier, P. (2014). Dissipation Rate Estimates from Microstructure and Finescale Internal Wave Observations along the A25 Greenland–Portugal OVIDE Line. *Journal of Atmospheric and Oceanic Technology*, *31*(11), 2530–2543. doi: 10.1175/JTECH-D-14-00036.1

García-Ibáñez, M. I., Pardo, P. C., Carracedo, L. I., Mercier, H., Lherminier, P., Ríos, A. F., & Pérez, F. F. (2015). Structure, transports and transformations of the water masses in the Atlantic Subpolar Gyre. *Progress in Oceanography*, *135*, 18–36. doi: 10.1016/j.pocean.2015.03.009

Garrett, C. (2001). Stirring and Mixing: What are the Rate-Controlling Processes? *Stirring to mixing in a stratified ocean. Proceedings Hawaiian Winter Workshop [12th] Held in the University of Hawaii at Manoa.*

Ijichi, T., St. Laurent, L., Polzin, K. L., & Toole, J. M. (2020). How Variable Is Mixing Efficiency in the Abyss? *Geophysical Research Letters*, *47*(7), e2019GL086813. doi: 10.1029/2019GL086813

Joyce, T. M. (1977). A Note on the Lateral Mixing of Water Masses. *Journal of Physical Oceanography*, *7*(4), 626 – 629. doi: 10.1175/1520-0485(1977)007⟨0626:ANOTLM⟩2.0.CO;2

Lauderdale, J. M., Bacon, S., Naveira Garabato, A. C., & Holliday, N. P. (2008). Intensified turbulent mixing in the boundary current system of southern Greenland. *Geophysical Research Letters*, *35*(4), L04611. doi: 10.1029/2007GL032785

Lazier, J., Hendry, R., Clarke, A., Yashayaev, I., & Rhines, P. (2002). Convection and restratification in the Labrador Sea,. *Deep Sea Research Part I: Oceanographic Research Papers*, *49*, 1819–1835.

Le Bras, I. A., Straneo, F., Holte, J., De Jong, M. F., & Holliday, N. P. (2020). Rapid Export of Waters Formed by Convection Near the Irminger Sea's Western Boundary. *Geophysical Research Letters*, *47*(3), e2019GL085989. doi: 10.1029/2019GL085989

Lee, M.-M., Marshall, D. P., & Williams, R. G. (1997). On the eddy transfer of tracers: Advective or diffusive? *Journal of Marine Research*, *55*(3), 483–505. doi: 10.1357/0022240973224346

Lherminier, P., Mercier, H., Huck, T., Gourcuff, C., Perez, F. F., Morin, P., ... Falina, A. (2010). The Atlantic Meridional Overturning Circulation and the subpolar gyre observed at the A25-OVIDE section in June 2002 and 2004. *Deep-Sea Research I*, *57*(11), 1374–1391. doi: 10.1016/j.dsr.2010.07.009

Lherminier, P., Velo, A., Perez, F. F., Le Bihan, C., Hamon, M., Le Bot, P., ... Lasa Gonzales, A. (2023). *BOCATS2 2023 Cruise data along the A25-OVIDE section.* SEANOE. Retrieved from `https://www.seanoe.org/data/00844/95607/` doi: 10.17882/95607

Lozier, M. S., Li, F., Bacon, S., Bahr, F., Bower, A. S., Cunningham, S. A., ... Zhao, J. (2019). A sea change in our view of overturning in the subpolar North Atlantic. *Science*, *363*(6426), 516–521. doi: 10.1126/science.aau6592

Mackay, N., Wilson, C., Holliday, N. P., & Zika, J. D. (2020). The Observation-Based Application of a Regional Thermohaline Inverse Method to Diagnose the Formation and Transformation of Water Masses North of the OSNAP Array from 2013 to 2015. *Journal of Physical Oceanography*, *50*(6), 1533–1555. doi: 10.1175/JPO-D-19-0188.1

Marsh, R. (2000). Recent Variability of the North Atlantic Thermohaline Circulation Inferred from Surface Heat and Freshwater Fluxes. *Journal of Climate*, *13*(18), 3239–3260. doi: 10.1175/1520-0442(2000)013⟨3239:RVOTNA⟩2.0.CO;2

Mauritzen, C. (1996). Production of dense overflow waters feeding the North Atlantic across the Greenland-Scotland Ridge. Part 1: Evidence for a revised circulation scheme. *Deep Sea Research Part I: Oceanographic Research Papers*, *43*(6), 769–806. doi: 10.1016/0967-0637(96)00037-4

Naveira Garabato, A. C., MacGilchrist, G. A., Brown, P. J., Evans, D. G., Meijers, A. J. S., & Zika, J. D. (2017). High-latitude ocean ventilation and its role in Earth's climate transitions. *Philosophical Transactions of the Royal Society A: Mathematical, Physical and Engineering Sciences*, *375*(2102), 20160324. doi: 10.1098/rsta.2016.0324

Naveira Garabato, A. C., Polzin, K. L., Ferrari, R., Zika, J. D., & Forryan, A. (2016). A Microscale View of Mixing and Overturning across the Antarctic Circumpolar Current. *Journal of Physical Oceanography*, *46*(1), 233–254. doi: 10.1175/JPO-D-15-0025.1

Oakey, N. S. (1982). Determination of the Rate of Dissipation of Turbulent Energy from Simultaneous Temperature and Velocity Shear Microstructure Measurements. *J. Phys. Oceanogr*, *12*(3), 256–271.

Orúe-Echevarría, D., Polzin, K. L., Naveira Garabato, A. C., Forryan, A., & Pelegrí, J. L. (2023). Mixing and Overturning Across the Brazil-Malvinas Confluence. *Journal of Geophysical Research: Oceans*, *128*(5), e2022JC018730. doi: 10.1029/2022JC018730

Osborn, T. R. (1980). Estimates of the local rate of vertical diffusion from dissipation measurements. *Journal of Physical Oceanography*, *10*, 83–89. doi: 10.1175/1520-0485(1980)010⟨0083:EOTLRO⟩2.0.CO;2

Osborn, T. R., & Cox, C. S. (1972, January). Oceanic fine structure. *Geophysical Fluid Dynamics*, *3*(1), 321–345. doi: 10.1080/03091927208236085

Petit, T., Lozier, M. S., Josey, S. A., & Cunningham, S. A. (2020). Atlantic Deep Water Formation Occurs Primarily in the Iceland Basin and Irminger Sea by Local Buoyancy Forcing. *Geophysical Research Letters*, *47*(22), e2020GL091028. doi: 10.1029/2020GL091028

Piccolroaz, S., Fernández-Castro, B., Toffolon, M., & Dijkstra, H. A. (2021). A multi-site, year-round turbulence microstructure atlas for the deep perialpine Lake Garda. *Scientific Data*, *8*(1), 188. doi: 10.1038/s41597-021-00965-0

Pickart, R. S., Straneo, F., & Moore, G. W. K. (2003). Is Labrador Sea Water formed in the Irminger basin? *Deep-Sea Research I*, *50*(1), 23–52. doi: 10.1016/S0967-0637(02)00134-6

Pradal, M.-A., & Gnanadesikan, A. (2014). How does the Redi parameter for mesoscale mixing impact global climate in an Earth System Model? *Journal of Advances in Modeling Earth Systems*, *6*, 586–601. doi: 10.1002/2013MS000273

Prandke, H., & Stips, A. (1998). Test measurements with an operational microstructure-turbulence profiler: Detection limit of dissipation rates. *Aquat. Sci.*, *60*(3), 191–209. (ISBN: 1015-1621) doi: 10.1007/s000270050036

Pérez, F. F., Mercier, H., Vázquez-Rodríguez, M., Lherminier, P., Velo, A., Pardo, P. C., ... Ríos, A. F. (2013). Atlantic Ocean CO2 uptake reduced by weakening of the meridional overturning circulation. *Nature Geoscience*, *6*(2), 146–152. doi: 10.1038/ngeo1680

Robbins, P. E., Price, J. F., Owens, W. B., & Jenkins, W. J. (2000). The Importance of Lateral Diffusion for the Ventilation of the Lower Thermocline in the Subtropical North Atlantic. *Journal of Physical Oceanography*, *30*, 67–89.

Roemmich, D. (2019). On the Future of Argo: A Global, Full-Depth, Multi-Disciplinary Array. *Frontiers in Marine Science*, *6*, 439. doi: 10.3389/fmars.2019.00439

Spingys, C. P., Williams, R. G., Tuerena, R. E., Naveira Garabato, A., Vic, C., Forryan, A., & Sharples, J. (2021). Observations of Nutrient Supply by Mesoscale Eddy Stirring and Small-Scale Turbulence in the Oligotrophic

North Atlantic. *Global Biogeochemical Cycles*, *35*(12), e2021GB007200. doi: 10.1029/2021GB007200

St Laurent, o., & Schmitt, R. W. (1999). The Contribution of Salt Fingers to Vertical Mixing in the North Atlantic Tracer Release Experiment. *Journal of Physical Oceanography*, *29*(7), 1404–1424. doi: 10.1175/1520-0485(1999)029⟨1404:TCOSFT⟩2.0.CO;2

Straneo, F. (2006). On the Connection between Dense Water Formation, Overturning, and Poleward Heat Transport in a Convective Basin*. *Journal of Physical Oceanography*, *36*(9), 1822–1840. doi: 10.1175/JPO2932.1

Tooth, O. J., Johnson, H. L., Wilson, C., & Evans, D. G. (2023). Seasonal overturning variability in the eastern North Atlantic subpolar gyre: a Lagrangian perspective. *Ocean Science*, *19*(3), 769–791. doi: 10.5194/os-19-769-2023

Warren, B. A. (1983). Why is no deep water formed in the North Pacific? *Journal of Marine Research*, *41*, 327–347.

Waterhouse, A. F., MacKinnon, J. A., Nash, J. D., Alford, M. H., Kunze, E., Simmons, H. L., . . . Lee, C. M. (2014). Global Patterns of Diapycnal Mixing from Measurements of the Turbulent Dissipation Rate. *Journal of Physical Oceanography*, *44*(7), 1854–1872. doi: 10.1175/JPO-D-13-0104.1

Whalen, C. B. (2012). Spatial and temporal variability of global ocean mixing inferred from Argo profiles. *Geophysical Research Letters*, *39*, L18612. doi: 10.1029/2012GL053196

Xu, X., Rhines, P. B., & Chassignet, E. P. (2018). On Mapping the Diapycnal Water Mass Transformation of the Upper North Atlantic Ocean. *Journal of Physical Oceanography*, *48*, 2233–2258. doi: 10.1175/JPO-D-17-0223.1

Zou, S., Lozier, M. S., Li, F., Abernathey, R., & Jackson, L. (2020). Density-compensated overturning in the Labrador Sea. *Nature Geoscience*, *13*(2), 121–126. doi: 10.1038/s41561-019-0517-1

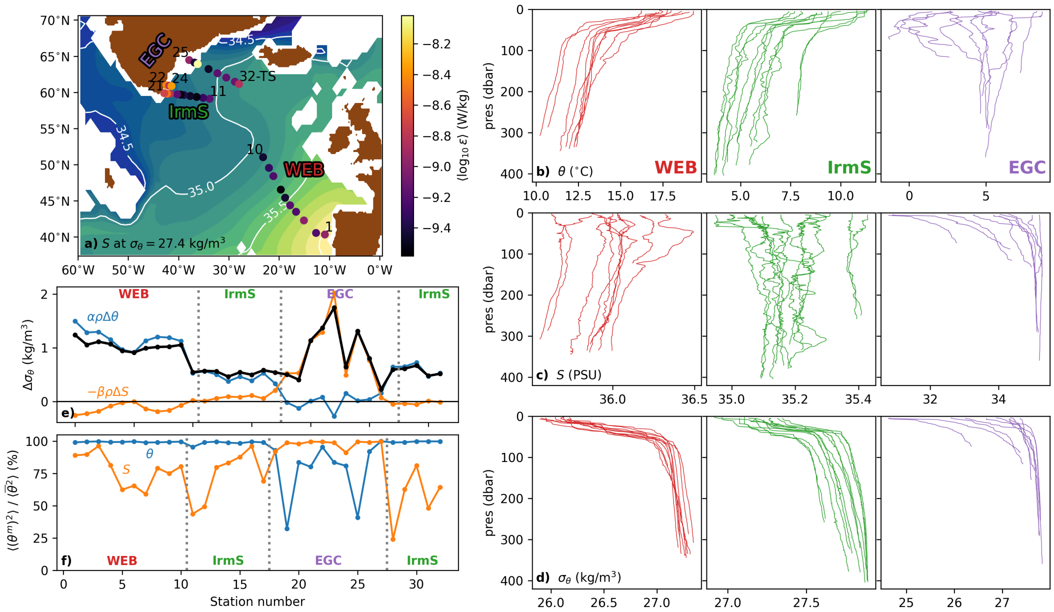

Figure 1. a) Map of the microstructure stations during the BOCATS2 cruise. Dots indicate the station positions and are color-coded by the mean value of ε below 50 m depth. Station numbers for the beginning and end of each sub-transect are shown, together with labels for the three analysis regions (Red: Western European Basin, WEB, stations 1-10; Green: Irminger Sea, IrmS, stations 11-17, 28-32; Purple: East Greenland Current, EGC, stations 18-27). The background contours represent the climatological salinity distribution at the $\sigma_\theta = 27.4$ kg/m^3 isopycnal based on the World Ocean Atlas 2018 (https://www.ncei.noaa.gov/access/world-ocean-atlas-2018/). Panels b), c), d) show one profile per station of potential temperature (θ), practical salinity (S) and potential density (σ_θ) color coded by region. Panel e) shows the top-to-bottom density difference at each station ($\Delta\sigma_\theta$, black), alongside partial contributions from temperature ($\alpha\rho\Delta\theta$) and salinity ($-\beta\rho\Delta S$). Panel f) shows the ratio between the variance of the mean-flow component of θ (and S), $\langle(\theta^m)^2\rangle$, to the total variance of the measured θ (and S) profiles, $\langle(\overline{\theta})^2\rangle$.

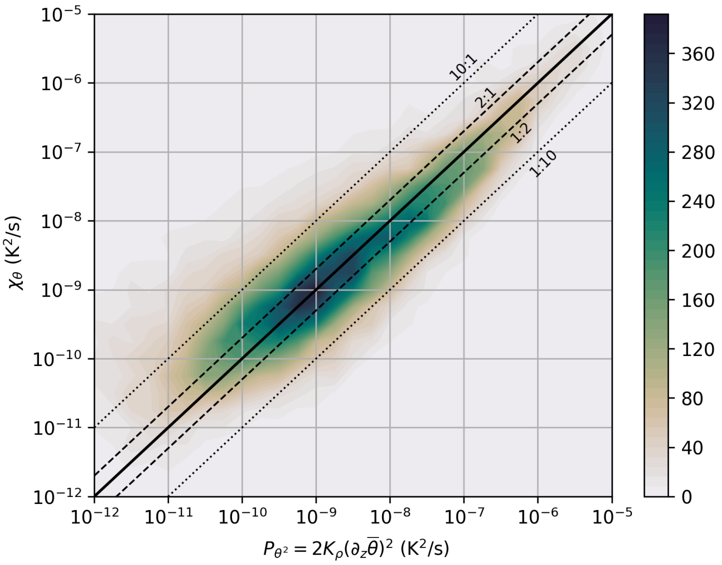

Figure 2. Two-dimensional histogram of thermal variance dissipation rate (χ_θ) and small-scale thermal variance production due to the action of small-scale turbulent motions on the fine-scale resolved potential temperature profile (P_{θ^2}), which includes the contributions from the mean flow and the mesoscale eddy components, in the context of the triple decomposition framework. The solid line indicates a one to one correspondence, and the dashed and dotted lines delimit agreement within a factor of 2 and 10, respectively.

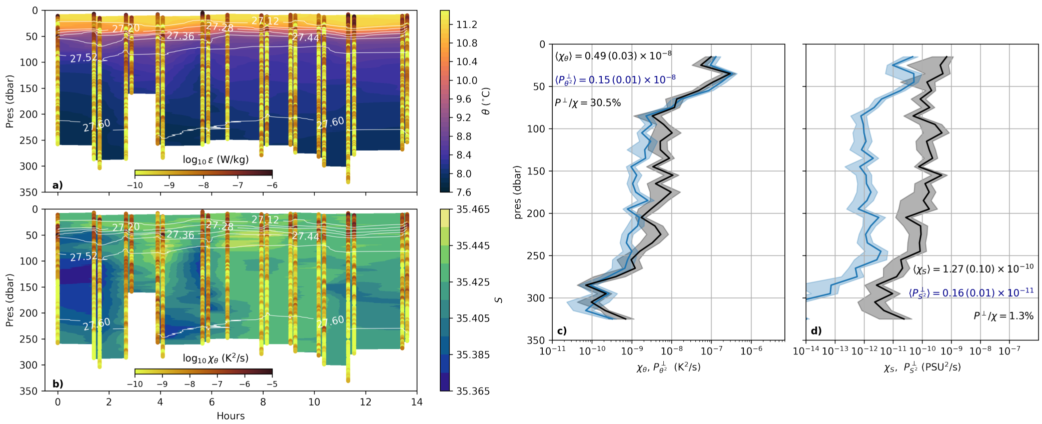

Figure 3. Time-series observation in station 32 over the Reykjanes Ridge. a) and b) show the 14-hours time-series of potential temperature (θ) and salinity (S) vertical profiles, with potential density contours (white) overlaid. Profiles of the dissipation rates of turbulent kinetic energy (ε) and thermal variance (χ_θ) are shown as colored dots. Panels c) and d) show the time-mean profiles of the dissipation rates of thermal and salinity variance (χ_θ, χ_S, black), along with small-scale variance production by small-scale turbulence ($P^{\perp}_{\theta^2}$, $P^{\perp}_{S^2}$, blue). Error bars (shading) represent ± 2 standard errors. Mean values of χ and $P^{\perp}$ below 100 m depth, and their ratio, are reported.

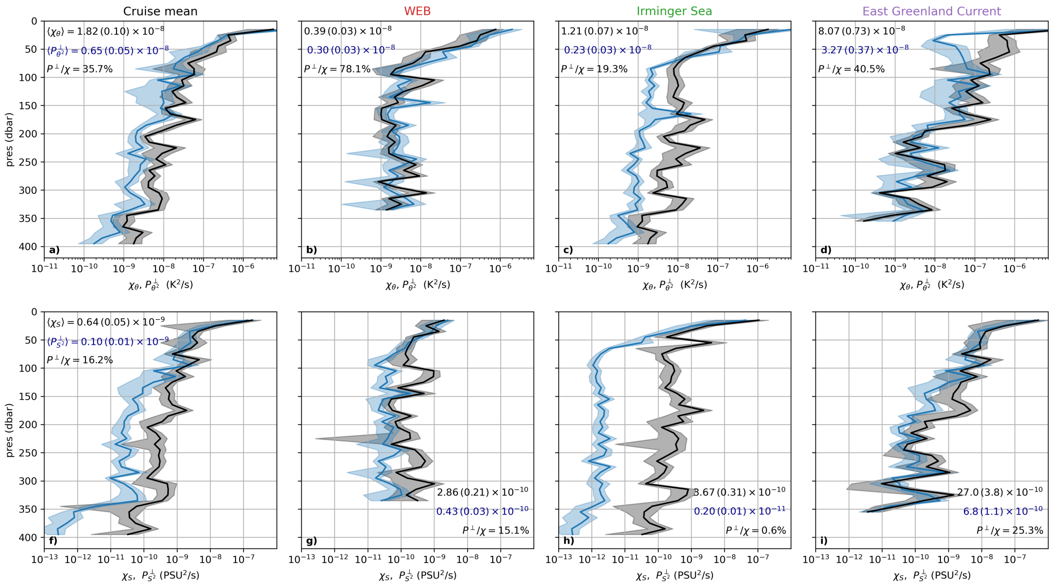

Figure 4. Mean profiles of the dissipation rates of thermal and salinity variance (χ_θ, χ_S, black), along with small-scale variance production by small-scale turbulence ($P^\perp_{\theta^2}$, $P^\perp_{S^2}$, blue) for the entire cruise (a, f), and for the different analysis regions: Western European Basin, WEB (b, g); Irminger Sea, IrmS (c, h); East Greenland Current, EGC (d, i). Error bars (shading) represent ± 2 standard errors. Mean values of χ and $P^\perp$ below 100 m depth, and their ratio, are reported.

Figure 1.

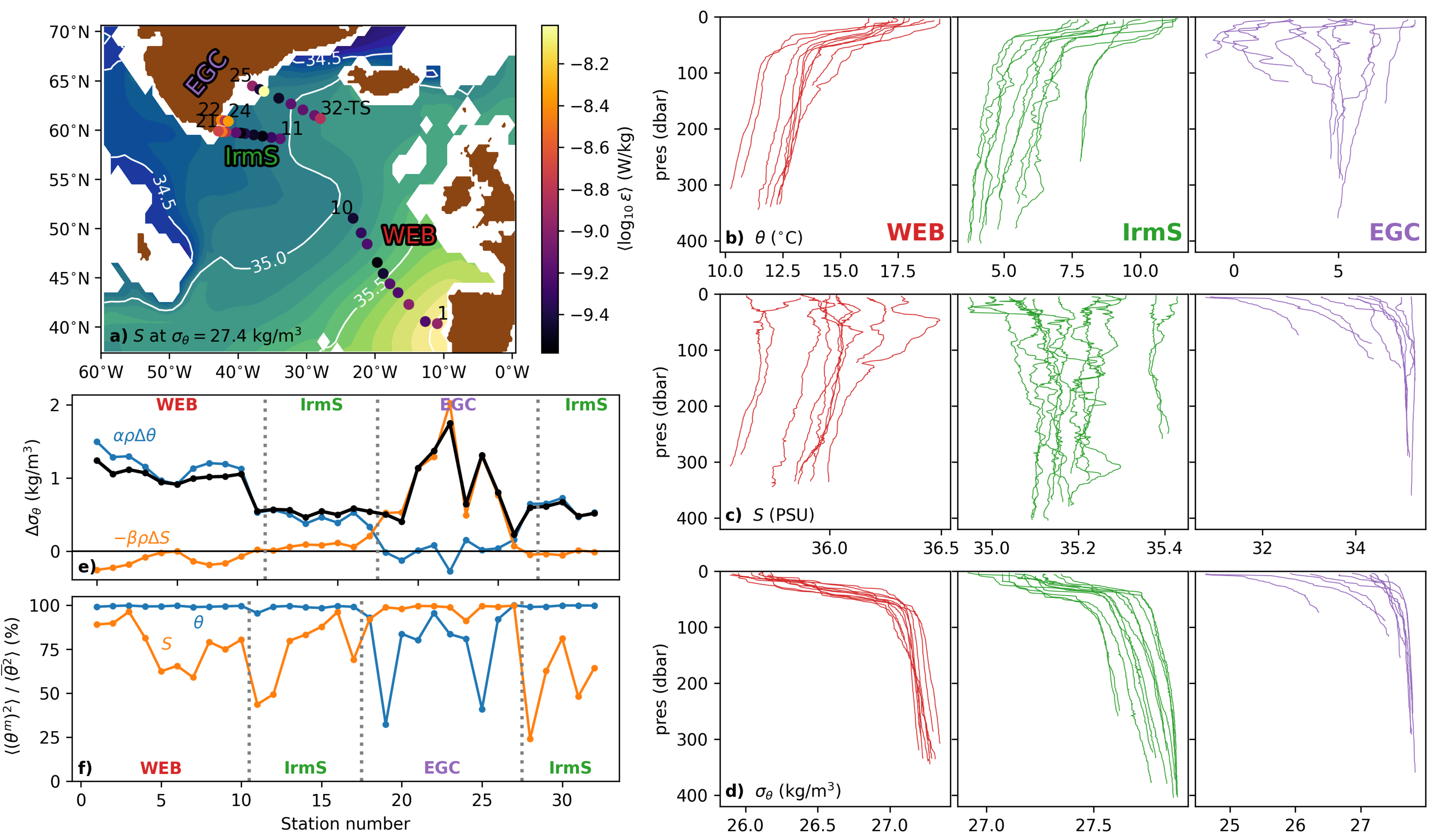

a) S at $\sigma_\theta = 27.4$ kg/m^3
EGC
IrmS
WEB
25
22
24
21
11
32-TS
10
1
34.5
35.0
35.5
$\langle \log_{10} \varepsilon \rangle$ (W/kg)
b) θ (°C)
c) S (PSU)
d) σ_θ (kg/m^3)
pres (dbar)
e)
$\alpha\rho\Delta\theta$
$-\beta\rho\Delta S$
$\Delta\sigma_\theta$ (kg/m^3)
f)
θ
S
$\langle(\theta^m)^2\rangle$ / $\langle\bar{\theta}^2\rangle$ (%)
Station number

Figure 2.

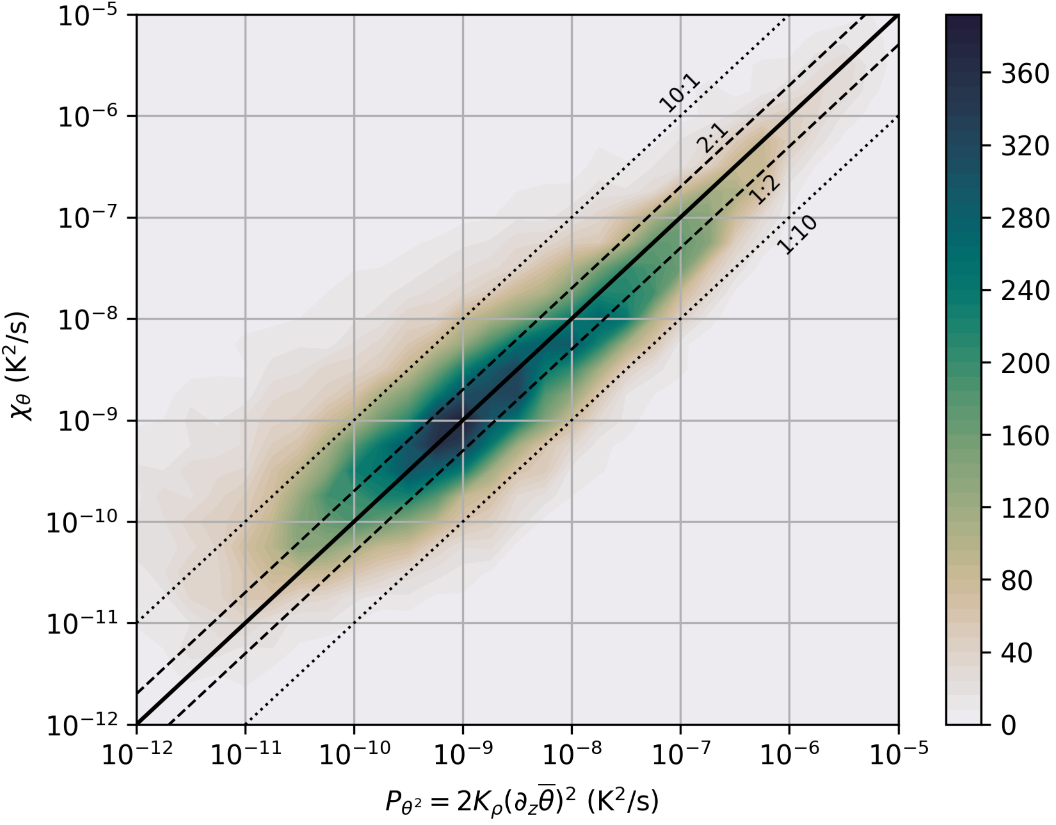

10:1
2:1
1:2
1:10
χ_θ (K^2/s)
$P_{\theta^2} = 2K_\rho(\partial_z\overline{\theta})^2$ (K^2/s)
10^{-12}
10^{-11}
10^{-10}
10^{-9}
10^{-8}
10^{-7}
10^{-6}
10^{-5}
0
40
80
120
160
200
240
280
320
360

Figure 3.

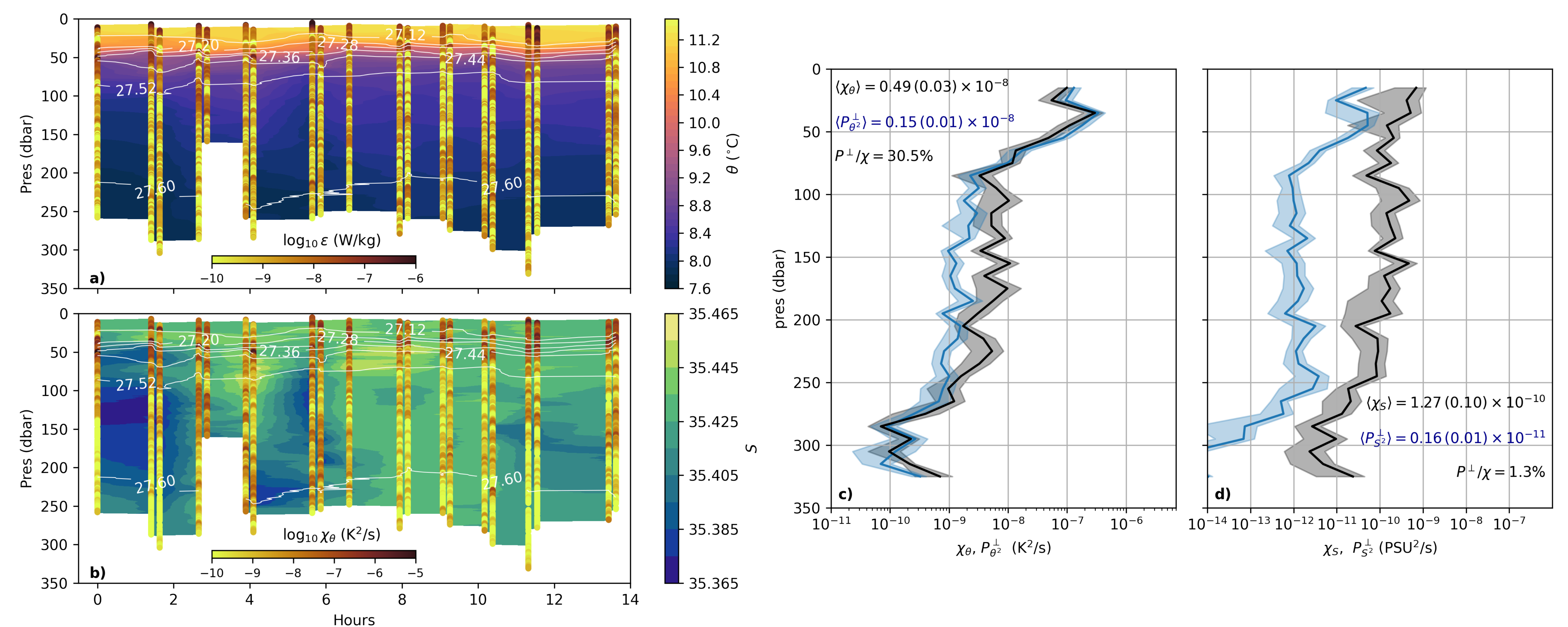

a)
b)
c)
d)
Pres (dbar)
Hours
θ (°C)
S
$\log_{10} \varepsilon$ (W/kg)
$\log_{10} \chi_\theta$ (K^2/s)
27.12
27.20
27.28
27.36
27.44
27.52
27.60
pres (dbar)
$\langle \chi_\theta \rangle = 0.49\,(0.03) \times 10^{-8}$
$\langle P^\perp_{\theta^2} \rangle = 0.15\,(0.01) \times 10^{-8}$
$P^\perp/\chi = 30.5\%$
$\langle \chi_S \rangle = 1.27\,(0.10) \times 10^{-10}$
$\langle P^\perp_{S^2} \rangle = 0.16\,(0.01) \times 10^{-11}$
$P^\perp/\chi = 1.3\%$
$\chi_\theta,\ P^\perp_{\theta^2}$ (K^2/s)
$\chi_S,\ P^\perp_{S^2}$ (PSU^2/s)

Figure 4.

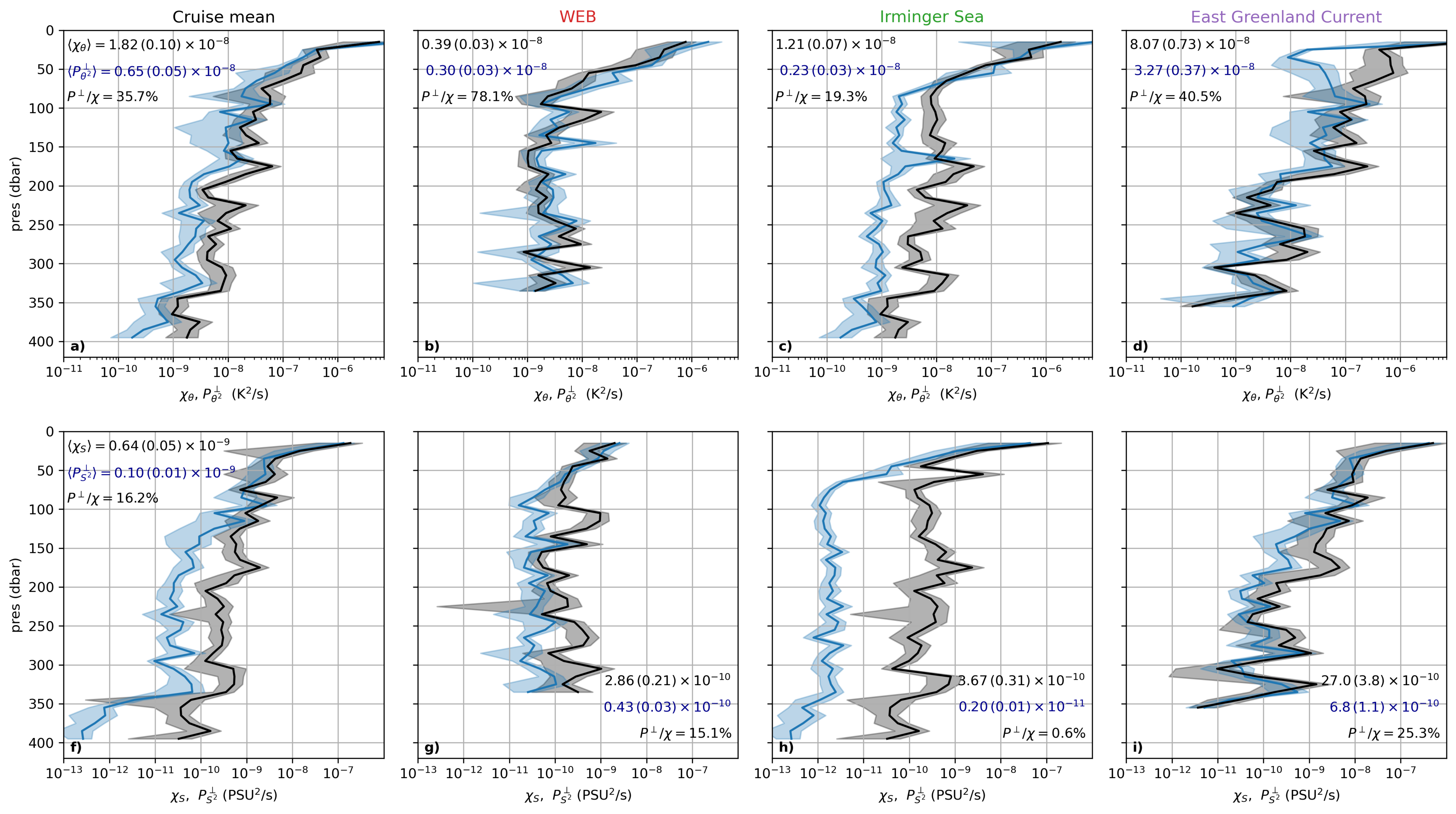

Cruise mean
WEB
Irminger Sea
East Greenland Current
$\langle\chi_\theta\rangle = 1.82\,(0.10)\times10^{-8}$
$\langle P^{\perp}_{\theta^2}\rangle = 0.65\,(0.05)\times10^{-8}$
$P^{\perp}/\chi = 35.7\%$
$0.39\,(0.03)\times10^{-8}$
$0.30\,(0.03)\times10^{-8}$
$P^{\perp}/\chi = 78.1\%$
$1.21\,(0.07)\times10^{-8}$
$0.23\,(0.03)\times10^{-8}$
$P^{\perp}/\chi = 19.3\%$
$8.07\,(0.73)\times10^{-8}$
$3.27\,(0.37)\times10^{-8}$
$P^{\perp}/\chi = 40.5\%$
a)
b)
c)
d)
pres (dbar)
$\chi_\theta,\ P^{\perp}_{\theta^2}$ (K^2/s)
$\langle\chi_S\rangle = 0.64\,(0.05)\times10^{-9}$
$\langle P^{\perp}_{S^2}\rangle = 0.10\,(0.01)\times10^{-9}$
$P^{\perp}/\chi = 16.2\%$
$2.86\,(0.21)\times10^{-10}$
$0.43\,(0.03)\times10^{-10}$
$P^{\perp}/\chi = 15.1\%$
$3.67\,(0.31)\times10^{-10}$
$0.20\,(0.01)\times10^{-11}$
$P^{\perp}/\chi = 0.6\%$
$27.0\,(3.8)\times10^{-10}$
$6.8\,(1.1)\times10^{-10}$
$P^{\perp}/\chi = 25.3\%$
f)
g)
h)
i)
$\chi_S,\ P^{\perp}_{S^2}$ (PSU^2/s)